ARTICLE   OPEN

Check for updates

Hierarchical optofluidic microreactor for water purification using an array of TiO$_2$ nanostructures

Hyejeong Kim[1,2,11 ✉], Hyunah Kwon[3,11], Ryungeun Song [4], Seonghun Shin[4], So-Young Ham[5], Hee-Deung Park[5,6], Jinkee Lee[4,7], Peer Fischer[3,8] and Eberhard Bodenschatz[2,9,10]

Clean water for human consumption is, in many places, a scarce resource, and efficient schemes to purify water are in great demand. Here, we describe a method to dramatically increase the efficiency of a photocatalytic water purification microreactor. Our hierarchical optofluidic microreactor combines the advantages of a nanostructured photocatalyst with light harvesting by base substrates, together with a herringbone micromixer for the enhanced transport of reactants. The herringbone micromixer further improves the reaction efficiency of the nanostructured photocatalyst by generating counter-rotating vortices along the flow direction. In addition, the use of metal-based substrates underneath the nanostructured catalyst increases the purification capacity by improving the light-harvesting efficiency. The photocatalyst is grown from TiO$_2$ as a nanohelix film, which exhibits a large surface-to-volume ratio and a reactive microstructure. We show that the hierarchical structuring with micro- to nanoscale features results in a device with markedly increased photocatalytic activity as compared with a solid unstructured catalyst surface. This is evidenced by the successful degradation of persistent aqueous contaminants, sulfamethoxazole, and polystyrene microplastics. The design can potentially be implemented with solar photocatalysts in flow-through water purification systems.

INTRODUCTION

Increased demand for clean water requires efficient strategies to purify water. Multiple water purification technologies have been developed, including physical processes or biochemical processes such as filtration, agglomeration, and desalination[1–3]. Among these, photocatalytic water purification is especially promising, given that photocatalysts are environmentally friendly materials that degrade or mineralize various pollutants with light being the only energy input. When a semiconductor catalyst absorbs photons with an energy equal to or greater than the band gap of the catalyst, photoexcited electron-hole pairs are generated. The reactions of electron-hole pairs with surrounding oxygen and water molecules form reactive oxygen species such as superoxide and hydroxyl radicals that could decompose organic chemicals and bioparticles into innocuous products such as CO$_2$ and H$_2$O[4–7].

The performance of water purification using photocatalysts is mainly dependent on photocatalytic efficiency and mass transfer efficiency. The former relates to light absorption and charge transport in photocatalysts, whereas the latter reflects the contact between the catalyst and the reactants, in addition to the removal of the products. To significantly enhance the photocatalytic efficiency, photocatalysts have been fabricated in various nanoscale geometric structures to provide large surface-to-volume ratios in the form of nanorods, nanotubes, and nanofibers using hydrothermal processes, sol-gel processes, or electrospinning[8–15]. However, the exchange with the catalyst is still limited as reactants and reaction products remain on the photocatalysts, which prevents further improvement of the water purification performance. To facilitate mass transfer efficiency, an optofluidic microreactor has been proposed, which combines microfluidics and photocatalysis[16–20]. While the solution is passed through the microfluidics channel, the photocatalyst causes a catalytic reaction to decompose various chemicals when exposed to light (Fig. 1a). The light and fluid in the optofluidic microreactor are characterized by a short molecular diffusion path, an intrinsically large surface-to-volume ratio, uniform illumination, and efficient light harvesting[21–25]. The light-harvesting can be further improved using nanostructures of photocatalysts that scatter light, or by modifying the base substrates to increase the optical path and thereby increase the number of electron-hole pairs that are generated due to multiple interactions with the photocatalyst[26,27]. In order to further enhance the performance of the optofluidic microreactor, which is dependent almost exclusively on diffusion, an innovative alternative is required to simultaneously increase the photocatalytic and mass transport efficiency.

In microfluidic channels, which generally are in the laminar flow regime due to low Reynolds numbers, efficient fluid mixing requires a chaotic flow produced by micromixers. A micromixer is a device based on mechanical microparts used to enhance the overall mixing capacity of the system by increasing the contact area between the reactants[28,29]. Based on the underlying principle, micromixers can be divided into two categories: active and passive. Active mixers use an external energy source to force the mixing of fluids inside the microchannel by electric, magnetic, or ultrasonic means. Passive mixers do not require external energy other than a pressure difference to drive the flow where the

[1]School of Mechanical Engineering, Korea University, Seoul 02841, Republic of Korea. [2]Max Planck Institute for Dynamics and Self-organization, Am Faßberg 17, 37077 Göttingen, Germany. [3]Max Planck Institute for Intelligent Systems, Heisenbergstr. 3, Stuttgart 70569, Germany. [4]School of Mechanical Engineering, Sungkyunkwan University, Suwon 16419, Republic of Korea. [5]School of Civil, Environmental and Architectural Engineering, Korea University, Seoul 02841, Republic of Korea. [6]KU-KIST Graduate School of Converging Science and Technology, Korea University, Seoul 02841, Republic of Korea. [7]Institute of Quantum Biophysics, Sungkyunkwan University, Suwon 16419, Republic of Korea. [8]Institute for Molecular Systems Engineering and Advanced Materials, Heidelberg University, INF 253, 69120 Heidelberg, Germany. [9]Institute for the Dynamics of Complex Systems, Georg-August-University Göttingen, 37073 Göttingen, Germany. [10]Laboratory of Atomic and Solid-State Physics and Sibley School of Mechanical and Aerospace Engineering, Cornell University, Ithaca, New York, NY 14853, USA. [11]These authors contributed equally: Hyejeong Kim, Hyunah Kwon. ✉email: h_kim@korea.ac.kr
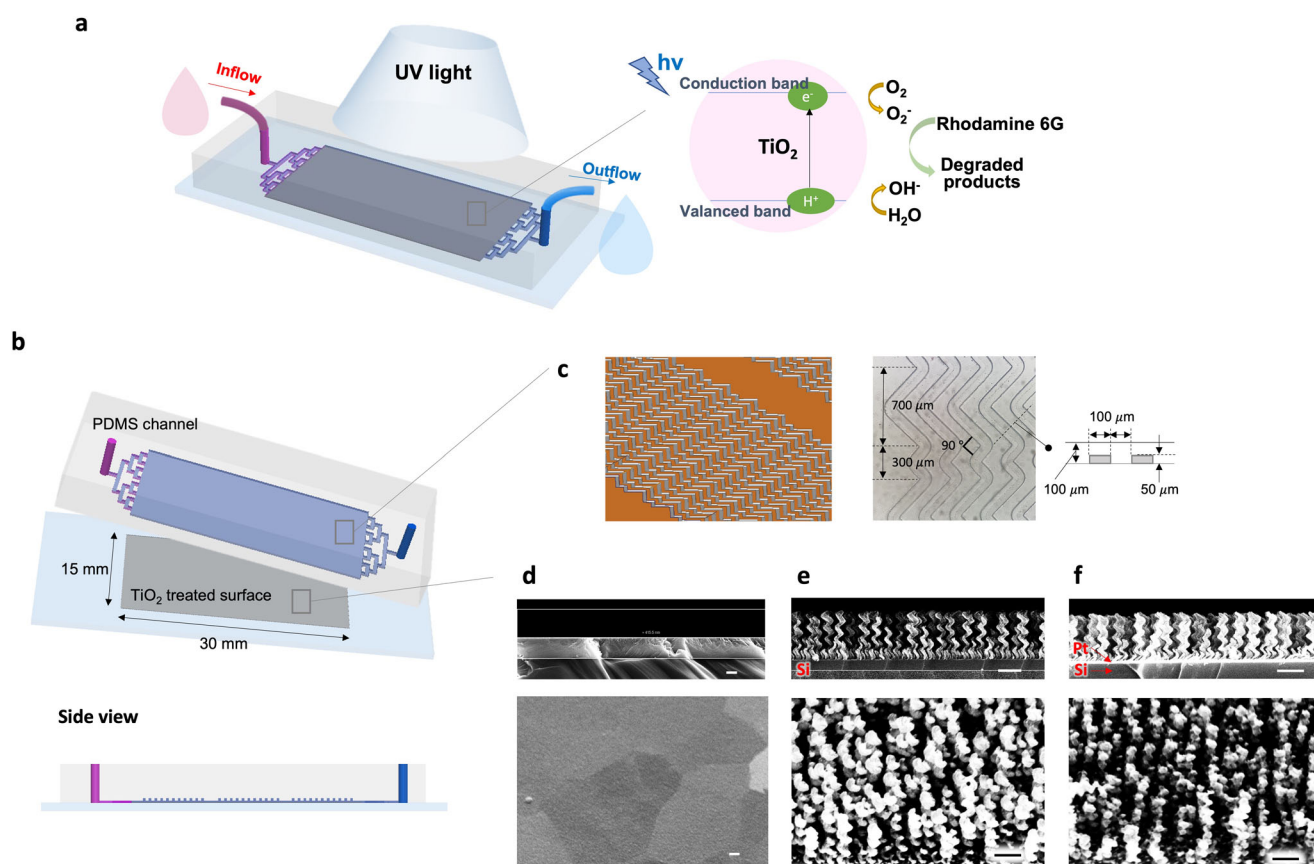
Fig. 1 Planar microreactor for photocatalytic water purification. a Schematic of a photocatalytic degradation experiment. Rhodamine 6 G (Rh6G) solution is introduced into the microreactor under UV illumination, and the Rh6G molecules in the solution are decomposed by photocatalysis at the bottom surface. **b** The microreactor has a rectangular reaction chamber consisting of a TiO_2 substrate at the bottom and a flat- or herringbone-structured polydimethylsiloxane (PDMS) slab on the TiO_2 substrate. **c** Geometry of the herringbone mixer. Scanning electron microscopy (SEM) images of TiO_2 surfaces with a **d** dense film (DF), **e** nanohelix (NH) structure, and **f** NH structure on platinum (Pt) substrate. (Upper) side view, (below) top view. Scale bar: 200 nm.

mixing is performed. In particular, mixing and transport is achieved by chaotic advection generated by complex micro-channel geometries, such as multidimensional structures, patterned groove structures, and split-and-recombination structures[29–33]. The patterning of the surfaces of the micromixer using specially designed microstructures is a common strategy for enhancing the mixing performance of a passive micromixer[34–36].

In this study, a planar photocatalytic microreactor that possesses hierarchical structures both at the micro- and nanoscale is presented for water purification using solar energy (Fig. 1b–f). Rhodamine 6 G (Rh6G) solution was used as a representative organic dye pollutant, which is highly corrosive and may have serious ecological effects on the aquatic environment[37,38]. When the Rh6G is degraded with a photocatalytic reaction, it is mineralized to carbon dioxide (CO_2) and water (H_2O), which are less toxic organic by-products that are environmentally benign. To maximize the water purification performance, the benefits of the nanostructured TiO_2 photocatalyst and the micromixer design of the channel were combined. The micromixer design with asymmetric herringbone-shaped grooves was applied to the microchannel to significantly speed up the mixing of the fluids in the low Reynolds number regime by inducing chaotic advection. The influence of the reactor's substrate on which photocatalysts were deposited, the structures of photocatalytic materials, the flow rate and the microscale geometry on the reaction efficiency were systematically investigated. Nanostructured TiO_2 photocatalysts were fabricated by a physical vapor shadow growth technique, also known as glancing angle deposition (GLAD),

which can produce highly porous nanostructured films on substrates. A numerical simulation of the flow inside the channel was carried out, allowing conclusions to be drawn about the hydrodynamic mechanism by which the reaction takes place in different cases. The result is an optimized design in which the nanostructures of the photocatalyst improve the water purification efficiency, while the herringbone micromixer further improves the reaction by creating a vortex along the reactor and thereby aids the molecular transport to and from the surface of the photocatalyst. Lastly, to demonstrate the capability of the reactor, more persistent contaminants, sulfamethoxazole, and polystyrene microplastics were successfully degraded. This study contributes to the systematic identification of the underlying physical mechanisms of the hierarchical design combining the nanoscale design of photocatalysts and the microscale design of mixer systems. In addition, the results of this study can contribute to providing solutions for more efficient water purification systems. The planar microreactor may also be of use in the general use of photocatalysts for energy applications as well as chemical and bioprocessing.

RESULTS AND DISCUSSION
The effects of the photocatalyst structures and the substrate materials on which the photocatalysts were deposited were studied using a planar photocatalytic microreactor that has the photocatalysts on one side and a flat microchannel on the other side. The effects of flow mixing on the reaction efficiency were
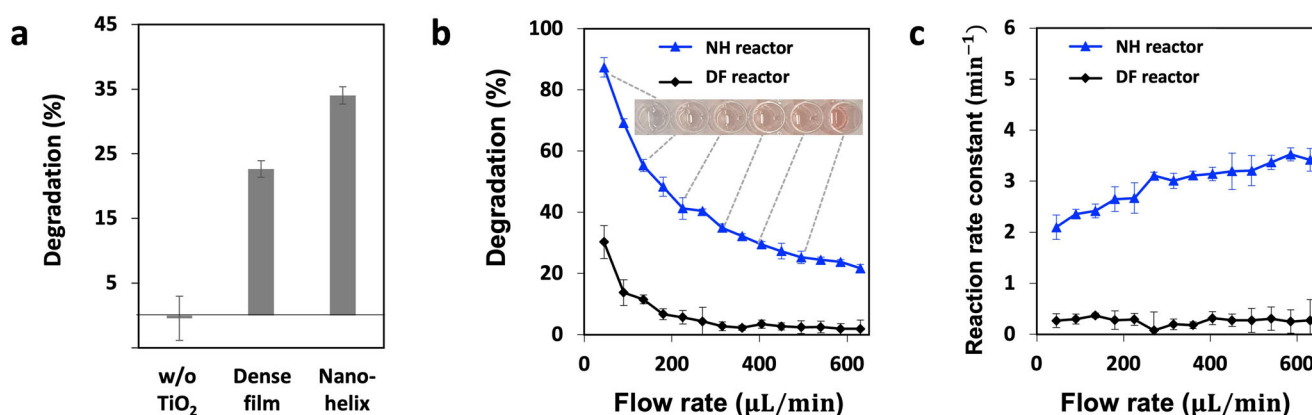
Fig. 2 Water purification capacity by photocatalytic degradation. a The Rh6G degradation of the cases without TiO$_2$, with dense TiO$_2$ film, and with TiO$_2$ nanohelix structures without flow for 90 min of UV-light illumination. **b** The Rh6G degradation and **c** reaction rate constant of the TiO$_2$ dense film-based microreactor (DF reactor) and TiO$_2$ nanohelix-based microreactor (NH reactor). Inset in B presents an optical image of the resultant purified Rh6G solutions injected at different flow rates. Gray dotted lines connect the corresponding flow rate. The error bars represent the standard deviations of at least five times repeated experiments.

further investigated using a microreactor possessing a micro-channel with herringbone grooves on top of the photocatalysts.

Enhancement of photocatalytic efficiency by helix nanostructure

To study the effects of the photocatalyst structure on water purification performance, two different types of substrates were prepared, one with a dense TiO$_2$ film (TiO$_2$ DF) and another with TiO$_2$ nanohelices (TiO$_2$ NHs). A TiO$_2$ DF and the TiO$_2$ NHs with respective thicknesses of 400 and 450 nm were formed on the Si substrate (Fig. 1d, e and Supplementary Figs. 1, 3). The TiO$_2$ NHs exhibited a porosity higher than 60% with a very high surface-to-volume ratio, as estimated from a linear effective medium approximation of the refractive index value of the film (Supplementary Fig. 2)[39]. In addition, the charge transport efficiency of the TiO$_2$ NHs is high, because of the near-single crystalline property, as confirmed in previous studies[40,41]. XRD and UV-Vis absorption spectra show that the TiO$_2$ in this study has anatase structures with an optical band gap of around 3.25 eV (Supplementary Figs. 4, 5). The XPS data reveals the two strong peaks from the TiO$_2$ NHs at around 465.5 and 459.8 eV, which are attributed to Ti $2p_{1/2}$ and Ti $2p_{3/2}$, and the peaks of O 1 s are located at about 531.0 eV, whose energy is equal to the O 1 s electron binding energy for TiO$_2$ (Supplementary Fig. 6).

In a stationary state without flow for 90 min, the TiO$_2$ NHs demonstrated the highest degradation (34.03 ± 1.32%), followed by the DF surface (22.66 ± 1.27%), whereas almost nothing was degraded without TiO$_2$ (Fig. 2a). Although TiO$_2$ NHs have a significantly larger surface area and fast charge transport properties, their degradation is only higher by a factor of ~1.5; thus, it is likely that the mass transport is the limiting factor for the degradation in the stationary state. Accordingly, an optofluidic microreactor was introduced to test this hypothesis and to improve the mass transfer by applying convection flow and thus increase the photocatalytic efficiencies.

We fabricated two optofluidic microreactors using an unstructured TiO$_2$ DF and TiO$_2$ NH substrates as reaction surfaces, respectively, and compared their water purification capabilities. The microreactors had a flat and rectangular reaction chamber consisting of TiO$_2$ DF or NHs substrates on one side and a flat PDMS microfluidic slab on the other side. The Rh6G solution was introduced into the TiO$_2$ dense film-based microreactor (DF reactor) and TiO$_2$ nanohelix-based microreactor (NH reactor) at various flow rates in the range of 45–630 μL/min. When the solution passed through the DF reactor under UV illumination, Rh6G molecules in the solution were decomposed by

photocatalysis at the bottom surface. Under these conditions, convection dominates as opposed to diffusion, considering the Péclet number $Pe = \frac{u h}{D}$ where u, h, and D are the flow velocity, channel height, and diffusion coefficient, respectively, which is a measure of the relative importance of convection between diffusion, of the system, ranged from 180–2500 when the diffusion coefficient of Rh6G in water was taken as $2.8 \times 10^{-6} cm^2/s$[42]. Given that the reaction of the photocatalyst occurs on the surface of the reactor, the reaction rate is relatively low in the case of a DF reactor with a small surface area. During the passage through the reactor, approximately 30% of the Rh6G was degraded at a low flow rate of 45 μL/min, and with an increase in the flow rate to 200 μl/min and higher, less than 10% of the Rh6G was decomposed (Fig. 2b). There was a decrease in the degradation with an increase in the flow rate, given that the residence time in the reactor was reduced accordingly. The reaction rate constant k, which refers to the purification capacity per unit time, was a low 0.26 ± 0.07 min^{-1} and almost constant, regardless of the flow rate (Fig. 2c). The TiO$_2$ nanohelix-based microreactor (NH reactor) demonstrated significantly improved water purification capacity than that of the DF reactor. At a low flow rate of 45 μl/min, almost all the dye molecules were degraded with 90% of the average degradation; and at a very high flow rate of 600 μL/min, the average decomposition efficiency was maintained at 21.6%. The reaction rate constant ranged from 2.10–3.42 min^{-1} with an increase in the flow rate from 45–630 μL/min. Compared with a DF reactor, the reaction rate constant of the NH reactor clearly exhibited a value that was higher by a factor of 13.23 on average. Please note that the reaction rate constant increased with an increase in the flow rate.

This result confirms that nanostructures of TiO$_2$ cause a remarkable improvement in the purification capacity in the photocatalytic reactor, and the convective flow resolves the mass transfer deficiency. The reaction capacity is determined mainly by two factors: the intrinsic photocatalytic efficiency and the external mass transfer efficiency of Rh6G from the liquid to the TiO$_2$ surface[43]. The intrinsic photocatalytic efficiency depends on the material properties and geometry of the TiO$_2$, and it is independent of the flow conditions. However, if the intrinsic photocatalytic efficiency is high, and critical reactants such as Rh6G, oxygen, and water necessary for the reaction are not exchanged quickly enough; the reaction efficiency is lowered[1]. This is indicated by the results, in that the reaction rate constant of the NH reactor was higher than that of the DF reactor under convection flow by a factor of approximately 13; whereas, in the stationary state, the degradation of the NHs was only 1.5 times
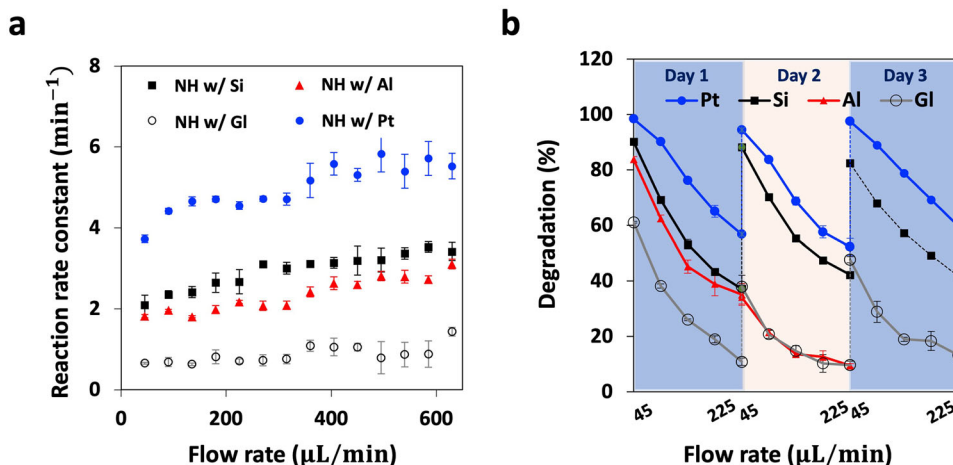
Fig. 3 Water purification capacities of NH reactors using different base substrates. a Reaction rate constant of the reactors with TiO$_2$ NHs deposited on the platinum (Pt), silicon (Si), aluminum (Al), and glass (Gl) substrates at different flow rates. **b** Re-usability of the NH reactors. The degradation efficiencies of the NH reactors with Pt, Si, Al, and Gl substrates were measured repeatedly on different 3 days at various flow rates. The error bars represent the standard deviations of at least six times repeated experiments.

higher. As is seen in Fig. 2c, the photocatalytic reaction rate constant of the flat surface, which has a lower reaction rate constant, to begin with, does not improve with the flow, whereas the TiO$_2$ nanohelix surface with a high reaction rate constant is significantly improved as the reactants are replenished by the flow.

Enhancement of photocatalytic efficiency by base substrates

The light-harvesting efficiency is a critical parameter for determining water purification performance. In microreactors, light is typically transmitted through a glass substrate, which causes some losses of solar energy. A dual-film optofluidic microreactor was proposed to enhance light harvesting by re-utilizing transmitted light at the bottom[10]. An alternative method involves the doubling of the optical path using reflective metallic substrates. It should be noted that TiO$_2$ photocatalysts can be coated on such metallic substrates; however, these may influence the phase and microstructure of the TiO$_2$, particularly for dense films, due to thermal stresses in the annealing process[44].

In this study, TiO$_2$ NHs were deposited on substrates, which are less influenced by thermal stress, given that each NH had a contact area of less than 50 nm with the substrate. We prepared four types of optofluidic flat microreactors with different base substrates, namely, glass (Gl) substrate, Silicon (Si) substrate, Aluminum coated substrate (Al substrate), and Platinum coated substrate (Pt substrate), on which the TiO$_2$ NHs were deposited; and thereafter investigated their effects on the water purification capacity at different flow rates under UV light. As shown in Fig. 3a, the NH reactors with Pt, Al, and Si substrates exhibited significantly higher performances than those with the Gl substrate. This is because a portion of the light is reflected from Pt, Al, and Si substrates to interact again with the NHs; whereas, most of the light is transmitted through or absorbed by the Gl substrates[45,46]. It should be noted that NH reactors with Pt and Si substrates exhibited higher efficiencies than those with Al substrates. Given that Al exhibits a significantly higher reflectivity, especially in the UV region, this was not expected. This is apparently due to the oxidation and degradation of Al in the measurement environment and confirmed by the re-usability test results. It should be noted that TiO$_2$ NHs deposited on Pt, Si, and Gl substrates can be reused multiple times, even after several days (Fig. 3b). However, in the case of Al substrate, the efficiency abruptly decreased upon re-use on the day after a single use. At the initial usage, 83.8% of the dye solution was decomposed at a low flow rate, and 35.1% at a high

flow rate. However, in the subsequent usage, it decreased to 34.2 and 9.5% at low and high flow rates, respectively. Therefore, Al is not a good candidate for water purification applications due to its oxidation.

There are very few studies that have tried to increase the light-harvesting efficiency of the optofluidic microreactor. Li et al. introduced a dual-film optofluidic microreactor with transparent glass as a base substrate, and a double-sided TiO$_2$ nanorod reactor showed improved performance compared to a single-sided reactor[10]. However, there are few reports of using base materials other than glass, and metal-based substrates in this study showed much-improved efficiency than glass substrates. Among those, the Pt-coated substrates demonstrated the highest performance with a reaction rate constant that was higher than that of the Si-coated substrate by ~2.5. Given that Pt and Si have similar UV reflectance values in the range of 300–400 nm, as employed for the proposed water degradation system[45,46], the Pt or Pt/TiO$_2$ NH interface could have an influence on water degradation. In particular, Pt can also function as a catalyst, thus resulting in a significantly higher photocatalytic efficiency. Furthermore, the internal photoemission, which describes the optically induced charge carrier transition at the interface, can play a role[47]. It is expected that a Schottky junction is formed at the interface of Pt and TiO$_2$ NHs. Considering the work function of Pt (5.8 eV) and the electron affinity of TiO$_2$ (4.0 eV), this results in a Schottky barrier height of approximately 1.8 eV[48,49]. Thus, photoexcited electrons from Pt can overcome the Schottky barrier under UV illumination and contribute to photogenerated charges in TiO$_2$[50].

Enhancement of mass transfer efficiency by herringbone micromixer

To further enhance the mass transfer efficiency, a herringbone micromixer was used in the reactors[51]. The water purification performances of the DF and NH reactors with the mixer were compared by measuring the Rh6G degradation capabilities of the reactors at various flow rates under UV-light illumination. In the case of the DF reactor, the degradation and reaction rate constant of the DF reactors with and without the mixer were almost identical, which suggests that the application of the mixer did not have a significant influence on the purification capacity. In the NH reactor, however, the mixer increased the degradation and reaction rate constant by 12 ± 5% and 17 ± 5% on average, respectively (Fig. 4). At a low flow rate of 45 μL/min, the NH reactor with the mixer degraded 88.9% of the Rh6G molecules in the
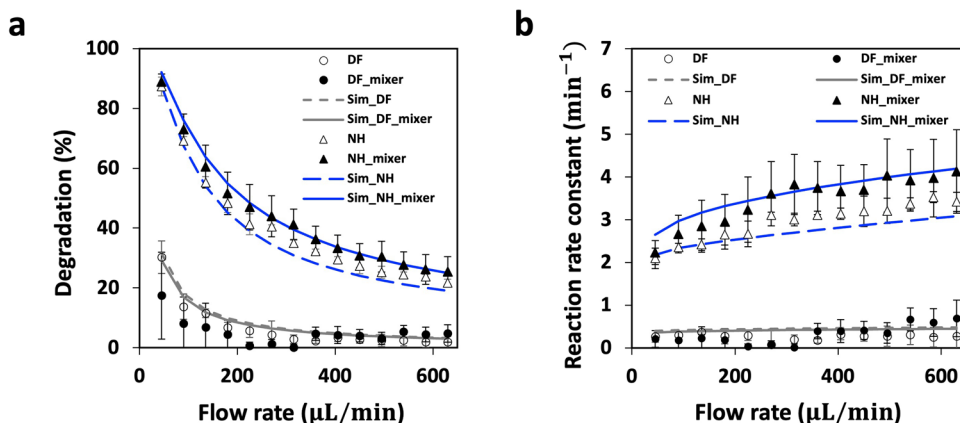
a

b

Fig. 4 Water purification capacity of DF and NH reactors when applying the herringbone micromixer. Comparison of the performance of **a** the Rh6G degradation and **b** the reaction rate constant of the DF and NH reactors at different flow rates. Filled markers and empty markers represent the experimental results of the microreactor covered with and without the herringbone mixer, respectively. The solid and dashed lines are the numerical simulation results. The error bars represent the standard deviations of at least ten times repeated experiments.

solution, which was 2% more efficient than in the absence of the mixer. At a higher flow rate of 630 µL/min, 25.3% of the molecules were degraded, which was 17% higher than that without the mixer. This increasing trend was clearly observed in the reaction rate constant, by which the mixer increased the reaction rate constant by 6% at a low flow rate of 45 µL/min, and 20% at a high flow rate of 630 µL/min. Thus, with an increase in the flow rate, there was a greater increase in the water purification performance of the herringbone mixer.

To determine the mechanism by which the herringbone mixer improved the water purification capacity, a finite element-based numerical simulation was performed to visualize the fluid flow behavior in the reactor. The Rh6G degradation within the DF reactor and NH reactor was simulated based on the same geometry, where the reaction rate constant of each surface was set differently, thus reflecting the intrinsic reaction rate. To simplify the problem, the entire microreactor was divided into smaller segments that represented the periodic structure of the entire herringbone mixer design. Thus, the segmented model of the herringbone mixer had a width of 1 mm and a length of 7.1 mm, which were 1/15 and 1/4 of the width and length of the entire channel, respectively. The model without the mixer had a rectangular channel with a width of 1 mm, length of 7.1 mm, and height of 100 µm. The Navier–Stokes equation for incompressible flow was used to simulate the convective flow-through the microchannel. The Reynolds numbers ($Re = \rho Uh/\mu$, where ρ, U, and μ are the density, velocity, and dynamic viscosity of the liquid, respectively, and h is the channel height) obtained in the study ranged from 0.038–0.5, thus indicating that the flow was in the laminar regime.

$$\rho \nabla \cdot \mathbf{u} = 0, \tag{1}$$

$$\rho \frac{\partial \mathbf{u}}{\partial t} + \rho(\mathbf{u} \cdot \nabla)\mathbf{u} = \nabla \cdot \left[-p\mathbf{I} + \mu(\nabla \mathbf{u} + (\nabla \mathbf{u})^T) \right] \tag{2}$$

where $\mathbf{u}$ and $\mathbf{I}$ are the flow velocity vector and unit vector, respectively, p is the pressure, and t is the time. The density ($=997$ kg/m^3) and viscosity ($=1$ mPa·s) were set the same as those of water at 25 °C. The fully developed flow was supplied to the inlet at a flow rate (Q) of 45–630 µL/min towards the outlet ($p = 0$) on the opposite side. A no-slip boundary condition ($\mathbf{u} = 0$) was applied to the upper and lower walls of the channel, and periodic conditions ($\mathbf{u}_1 = \mathbf{u}_2$ and $p_1 = p_2$, where subscripts 1 and 2 indicate each side wall) were applied to both sides of the channel.

The change in the concentration of the solution passing through the microchannel was calculated using the following convection–diffusion equation:

$$\frac{\partial c}{\partial t} = \nabla \cdot (D\nabla c) - \nabla \cdot (\mathbf{u}c) + R \tag{3}$$

where c is the concentration of the solution, D is the diffusion coefficient of Rh6G in water ($= 2.8 \times 10^{-6}$ cm^2/s)[42], and R describes the sinks or sources of the concentration. The initial concentration was set to 0, and the liquid with $c_0 = 1$ was supplied at the inlet and removed through the opposite outlet ($\mathbf{n} \cdot D\nabla c = 0$, where $\mathbf{n}$ is a normal vector for the outlet). The flux ($\mathbf{J}$) was zero on the upper wall ($\mathbf{n} \cdot \mathbf{J} = 0$), and periodic boundary conditions were applied to the side walls ($-\mathbf{n}_1 \cdot \mathbf{J}_1 = \mathbf{n}_2 \cdot \mathbf{J}_2$). On the bottom surface, the concentration decreased at the following N^{th} order rate by the following chemical reaction with TiO$_2$:

$$-\mathbf{n} \cdot D\nabla c = k \cdot c^N \tag{4}$$

where k denotes the catalyst activity. Moreover, k and N were used as fitting parameters to match the numerical results with the experimental results. Given that the entire microreactor channel was longer than the segment used for the numerical model by a factor of four, four iterations were repeated using the velocity field and concentration distribution at the outlet as the boundary conditions at the inlet of the subsequent iteration. The average concentration at the outlet of the previous iteration was used to calculate the degradation and the reaction rate constant.

The degradation was computed according to various reaction rates by changing the fitting parameters N and k in Eq. (4) to compare the numerical and experimental results (Fig. 4a). The empirical parameters were obtained from the simulation, as follows: $N = 1.2$, $k = -8 \times 10^{-7}$ (for the DF reactor), and -1.05×10^{-5} (for the NH reactor). The abovementioned parameters clarify the experimental results for the cases without and with the mixer, respectively, where the NH reactor had a reaction rate constant k that was higher than that of the DF reactor by a factor of ~13 (Fig. 2c). The mixer of the NH reactor increased the reaction rate constant by 22% at a low flow rate of 45 µL/min, and by 36% at a high flow rate of 630 µL/min. Moreover, there was almost no change in the value of the DF reactor in the cases with and without the mixer, thus indicating a similar trend to that of the experimental results (Fig. 4b).

The flow behavior of the fluid in the reactor helps clarify the influence of the herringbone mixer on the reaction efficiency, which strongly depends on the mass transfer of reactants from the solution to the photocatalyst surface. As illustrated in Fig. 5a, as there was no flow along the Z axis inside the reactor without the mixer, the transport of Rh6G from the upper region to the bottom
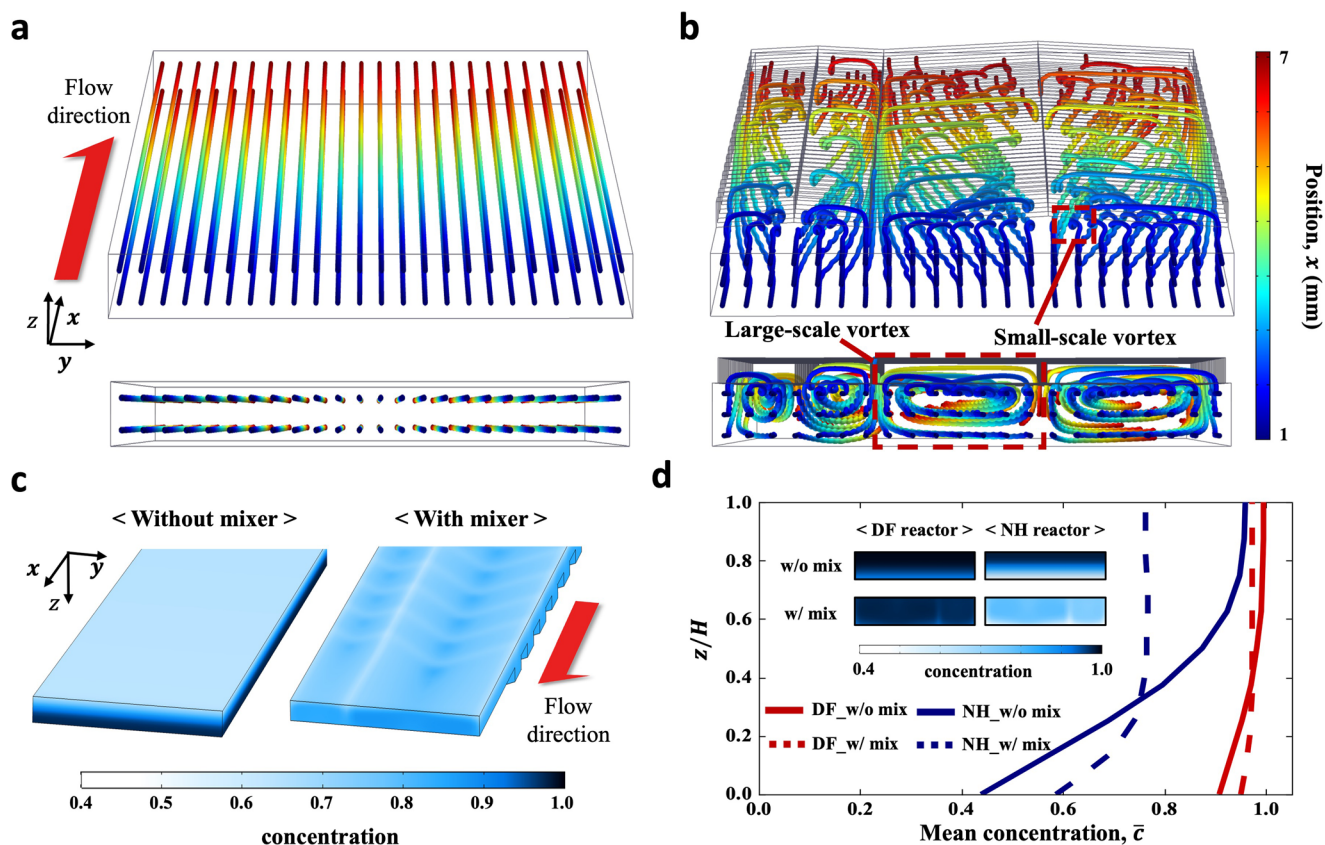
Fig. 5 Comparison of streamlines within the microreactor. a Without and **b** with the herringbone mixer. **c** Bottom side view of Rh6G concentration distribution near the outlet of the microreactor without/with the mixer. **d** Concentration profile of Rh6G at the outlet of the microreactors. The mean concentration ($\bar{c}$) is the average value of the concentration at each height (z/H). The inset images illustrate the concentration distribution at the outlet.

surface was primarily dependent on diffusion. Relatively weak diffusion when compared with convection in microreactors, as indicated by the high Péclet number ($180 < Pe < 2500$), results in a steep concentration gradient along the Z axis of the channel (Fig. 5c, d; without mixer cases with bold lines). The lowered concentration near the TiO_2 bottom surface, which represents the deficiency of the reactants, could limit the reaction rate and reduce the Rh6G degradation. Moreover, the herringbone mixer generated four counter-rotating vortices along the flow direction in a laminar regime, with a primary large-scale vortex along the main channel, followed by a small-scale secondary vortex on the channel wall at the end (Fig. 5b). Given that the vortices could mix Rh6G from the upper to the bottom of the reactor, the mixer flattened the concentration gradient along the Z axis (Fig. 5c, d; mixer cases with dotted lines) and increased the reaction rate accordingly by eliminating the deficiency problem.

In the DF reactor, the degradation and the reaction rate constant changed slightly, even with the addition of the mixer, whereas the NH reactor further enhanced the purification by the mixer (Fig. 4a). In the DF reactor with a low intrinsic reaction rate, the concentration gradient of the reactants throughout the reactor was low, where a high concentration of 90% or more reactants was present at the bottom of the reactor, leaving no space for the mixer to effectively improve the reaction performance (Fig. 5d). If the active reaction of the catalytic surface leads to a shortage of the reactants, as indicated by the steep concentration gradient of the NH reactor with the mixer, the vortex generated by the herringbone mixer significantly improves the reaction performance by increasing the available reactants to the catalyst and removing the reacted products from the catalyst.

Decomposition of various aquatic pollutants

To show the capability of our device to degrade various water pollutants, photocatalytic degradations of cationic dye Methyl orange (MO) and more persistent contaminants, sulfamethoxazole (SMX) and polystyrene (PS) microplastic were investigated[52–55].

The MO solution was introduced into the TiO_2 nanohelix-based microreactor (NH reactor) at various flow rates in the range of 45–630 μL/min under UV illumination. During the passage through the reactor, approximately 30% of the MO was degraded at a low flow rate of 45 μL/min, and with an increase in the flow rate to 630 μL/min, less than 5% of the MO was decomposed (Fig. 6a and Supplementary Fig. 8). The reaction rate constant, k, was a 0.27 ± 0.06 min^{-1} in average (Supplementary Fig. 8C). Although the degradation efficiency was lower than that of the anionic dye Rh6G, it showed a relatively high degradation potential. SMX is an antibiotic that has been consistently detected in wastewater and is necessary to be removed in order to avoid an increase in antibiotic resistance in humans. In the absence of flow, SMX was hardly decomposed with TiO_2 NHs. Next, the SMX solution was introduced into the TiO_2 NH reactor at various flow rates in the range of 9–180 μL/min under UV illumination. With the NH reactor, approximately 28% of the SMX was degraded at a low flow rate of 9 μL/min, and with an increase in the flow rate above 45 μL/min, less than 5% of the SMX was decomposed (Fig. 6b). Lastly, since the existing sewage treatment system cannot catch all microplastics, they can remain in the water for a long time, be absorbed by aquatic organisms, travel through the food chain, and finally act as a toxic substance to humans. In this vein, we demonstrated our present system is suitable for the degradation of microplastic, especially polystyrene (PS) microparticle. To study the performance of the PS particle degradation process, the
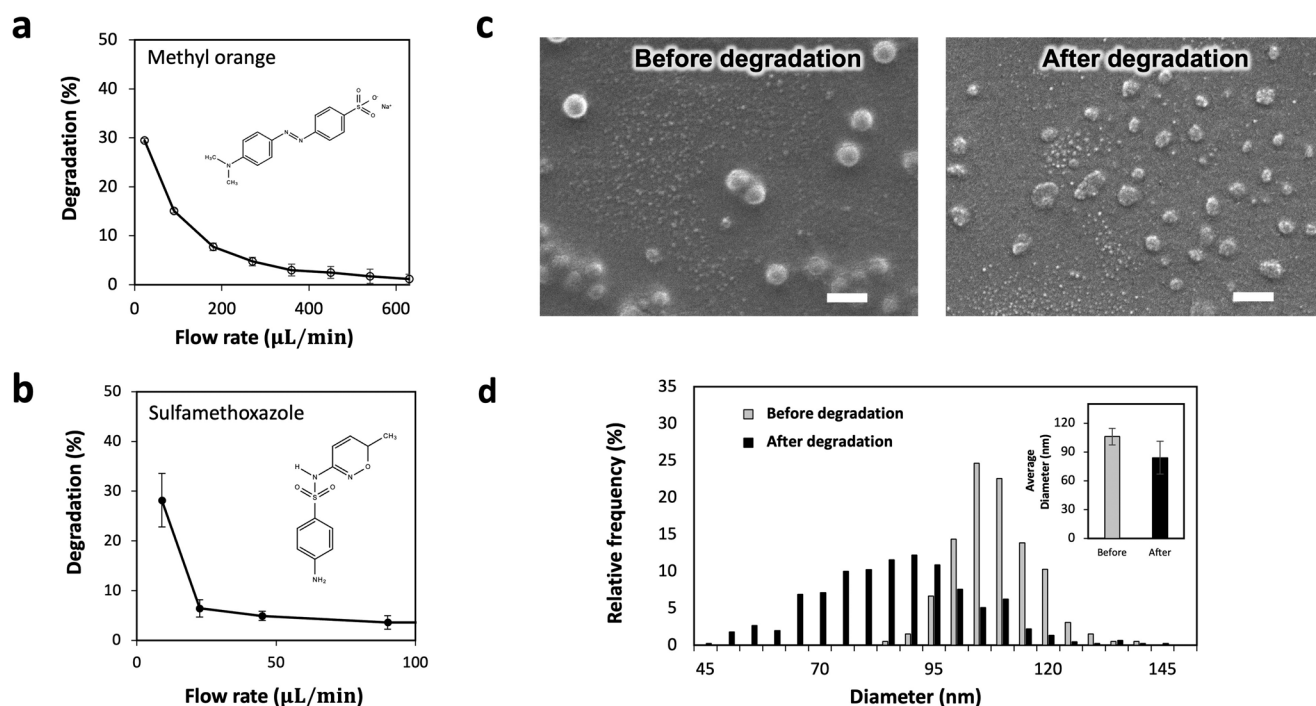
Fig. 6 Water purification capacity by photocatalytic degradation. a The MO degradation and **b** the SMX degradation of the TiO$_2$ nanohelix-based microreactor. The error bars represent the standard deviations of three samples. **c** SEM images of polystyrene particles before and after photocatalytic degradation. **d** PS particle diameter distribution before and after degradation. The inset shows the average diameter of the particles. Scale bar: 200 nm.

Table 1. Reaction rate constants for various types of microreactors at low and high flow rates.				
Reactor type	Photocatalyst structure	Base material	Reaction rate constant	
			Low flow rate (45 µL/min)	High flow rate (630 µL/min)
Flat microreactor	Dense film	Silicon	0.27 ± 0.14	0.27 ± 0.41
	Nanohelix	Silicon	2.10 ± 0.24	3.42 ± 0.22
		Platinum	3.73 ± 0.09	5.52 ± 0.32
		Aluminum 1cycle	1.82 ± 0.07	3.11 ± 0.12
		2cycle	0.42 ± 0.04	0.62 ± 0.12
		Glass	0.66 ± 0.02	1.44 ± 0.11
Herringbone microreactor	Dense film	Silicon	0.21 ± 0.19	0.69 ± 0.43
	Nanohelix		2.23 ± 0.28	4.13 ± 0.97
The error estimates represent the standard deviations of at least five to ten times repeated experiments.				

photodegradation of standard polystyrene latex suspension, which was employed as the microplastic model, with $3.79 \pm 0.23 \times 10^8$ particles/mL in Deionized water was examined. The PS particle solution was introduced into the microreactor with a flow rate of 2.25 µL/min by a syringe pump, and the photocatalytic reaction was carried out under UV-light illumination. The degraded PS particle solution was collected from the outlet of the microreactor, and their morphologies are observed by SEM. As a result, PS particles were clearly degraded in NH reactor, where the average size of the particle decreased from 106.03 ± 8.79 nm to 84.06 ± 17.19 nm (Fig. 6c, d).

Compared to the previous studies, where the degradation of the SMX or PS particle took several hours to days, our system showed relatively fast degradation, where the residence time of SMX and PS particles in the reactor were only around 5 and 20 min with a flow rate of 9 and 2.25 µL/min, respectively[54,56–58]. These

results suggest that our system performs very well in removing water pollutants.

A hierarchical photocatalytic microfluidic reactor was designed and characterized for the photodegradation of Rh6G under UV irradiation. Table 1 summarizes the reaction rate constants for all types of microreactors at low and high flow rates. This study attempts to maximize water purification efficiency by simultaneously improving photocatalytic efficiency and mass transfer efficiency by combining the benefits of a nanostructured photocatalyst, light harvesting by base substrates, and a micromixer. The experimental results confirmed that the nanostructures of the nanohelix-based reactor enhanced the water purification capacity almost by 13 times under conditions of convective flow compared to the dense film-based reactor. The light-reflective metallic substrates also increased the purification capacity compared to the Gl substrate by enhancing the light-harvesting efficiency. In addition, the herringbone micromixer applied to the

nanohelix reactor further contributed to the water purification performance by up to 20% by generating a vortex along the reactor, which was qualitatively confirmed by a numerical simulation. We additionally confirmed that our reactor, with this improved purification performance, can decompose organic matters as well as more persistent contaminants by demonstrating the photocatalytic degradation of the cationic dye methyl orange, antibiotic sulfamethoxazole, and polystyrene microplastics. What would normally take hours or days for pollutants to decompose was accomplished in minutes with our reactor system. By systematically demonstrating the mechanisms governing the hierarchical design of nanoscale photocatalysts and micromixer systems, the findings of this study contribute to the smart design of an optofluidic microreactor with potential applications in the fields of energy, environmental science, and biomedicine.

In order for this solar-based water treatment system to be used in the field, some hurdles have to be overcome. First, the amount of water that can be purified needs to be increased, possibly by connecting the reactor systems in parallel or in series. In addition, using a photocatalyst that reacts not only with UV-light but also more efficiently across the entire solar spectrum will increase the utility of the system. Also, even if the reactor could be reused several times in this study, nanoscale photocatalysts need to be manufactured more robustly in the future to guarantee product stability. In natural water, there are various elements widely present, such as anions and humic acids, which could potentially retard the photocatalytic reaction by inhibiting the formation of free radicals, reducing light transmittance, or adsorbing to active sites of the photocatalyst. Therefore, in the future engineering design, if TiO$_2$ is to be applied for the treatment of wastewater in nature, the retardation effects of various substances in the natural environment should be concerned.

METHODS

The TiO$_2$ substrate preparation and characterization

Four base substrates were used: glass (Gl), silicon (Si), platinum (Pt), and aluminum (Al). For Gl substrates, microscope slides with a thickness of 1 mm were cleaned with acetone and isopropanol. The Si substrate was the wafer (boron doped, <100> orientation), cleaned in piranha solution (a mixture of three parts of concentrated H$_2$SO$_4$ and one part of 30% H$_2$O$_2$) for 30 min. For the metallic substrates, the piranha-cleaned Si wafers were first coated with a 5 nm thick Ti adhesion layer and then with a 20 nm thick Pt or Al layer (>99.99% purity) by e-beam evaporation. Thereafter, TiO$_2$ nanostructures were fabricated using the GLAD technique. In GLAD, the obliquely incident TiO$_2$ vapor flux produces small random islands of deposited TiO$_2$ material. Behind these clusters, the subsequent vapor flux cannot reach due to a shadowing effect[59]. This causes the film to grow by means of slanted nanorods with high porosity. Furthermore, a film of nanohelices could be produced by rotating the substrate during growth and by controlling the substrate rotation speed[59]. In this study, TiO$_2$ nanohelices (NHs) were fabricated with a substrate tilt angle of 87° at a deposition rate of 2 Å/s and a substrate rotation speed of 0.28 °/s. A TiO$_2$ dense film (DF), as a reference sample, was also fabricated with a vapor flux incident along the surface normal (tilt angle of 0°) and a deposition rate of 2 Å/s. All films were annealed at 500 °C for 2 h in ambient air to induce crystallization into the anatase phase.

X-ray photoelectron spectroscopy (XPS, PHI X-tool, ULVAC-PHI, Inc.) with Al (mono) X-rays (25.1 W) was used to detect the chemical combination state of TiO$_2$ NHs. Combined with the X-ray energy dispersive spectroscopy (EDX), scanning electron microscopy (SEM, Quanta 250 FEG; FEI Ltd.) was utilized to analyze the basic material compositions and visualize the morphologies of the NHs (Supplementary Figs. 1–3). The crystal structure of the NHs

was analyzed by X-ray diffraction (XRD). XRD was carried out using a Rigaku D/ MAX2500 with Cu Kα radiation (Supplementary Fig. 4). The UV-Vis measurements were performed in a Varian Cary 4000 UV-Vis spectrometer. UV-Vis spectra was measured using TiO$_2$ NHs on a double-side-polished sapphire substrate that is transparent in the region of the TiO$_2$ band edge (Supplementary Fig. 5).

Microreactor fabrication

The microreactor had a rectangular reaction chamber consisting of a TiO$_2$ substrate on one side and a flat or herringbone-structured polydimethylsiloxane (PDMS) on the other. (Fig. 1). The herringbone grooves with alternating permutation arrangements were designed to induce a chaotic flow for enhanced flow mixing. The master mold for the PDMS reactor was fabricated from acrylic material using a milling machine. To prototype the mold, a PDMS elastomer base and curing agent mixed at a ratio of 10:1 were cast on the molds and incubated in an oven at 75 °C for 2 h. The cured PDMS slab was peeled off, and holes with a diameter of 0.5 mm were punched at the inlet and outlet of the slab. After plasma treatment on the TiO$_2$ substrate and the PDMS slab, they were precisely aligned and bonded. Finally, tubes were connected to the inlet and outlet of the reactor, the inlet side tube was connected to a syringe pump for fluid injection.

The volumetric dimensions of the flat microreactor chamber were 1.5 cm (width) × 3.0 cm (length) × 100 μm (height) = 45 μL, and those of the herringbone reactor chamber were the same as the dimensions of the planar area. Moreover, the height was adjusted to ensure that the volume was the same as in the flat microreactor. The height of the herringbone groove was 50 μm, and the gap between the neighboring grooves was 100 μm. The angle between the longitudinal axis of the channel and the herringbone structure was 45°. The three-dimensional (3D) geometry and dimensions of the microfluidic chip are illustrated in Fig. 1. At the inlet and outlet, tree-branch-shaped microchannels were adopted to ensure a uniform flow over the entire reaction chamber.

Experimental setup for photocatalytic degradation

To study the performance of the water purification process, the photodegradation of 0.05 M Rhodamine 6 G (Rh6G, Sigma-Aldrich) dye solution, which was employed as the representative organic pollutant model, was examined under UV-light irradiation. For a reaction without flow, the TiO$_2$ dense film (DF) and TiO$_2$ nanohelix (NH) substrates covered with 3 mL of Rh6G solution were placed in a petri dish and irradiated with ultraviolet (UV) light (Altis uvcure, South Korea, 365 nm) for 90 min. As a comparison, only 3 mL of Rh6G solution without TiO$_2$ was also prepared and irradiated with the same UV-light. For the optofluidic reaction, Rh6G solution was added to the microreactor, and the photocatalytic reaction was carried out under UV-light illumination (310–390 nm, UVICO, Rapp OptoElectronic GmbH). The Rh6G solution was introduced into the device by a syringe pump (Harvard Apparatus, PHD 2000) and decomposed by photocatalysis while passing through the microreactor (Fig. 1a). The degraded Rh6G solutions were collected from the outlet of the microreactor, and their absorption spectra were analyzed using a UV–visible spectrophotometer (Sunrise, TECAN, Germany). The degradation of Rh6G was evaluated by monitoring the absorbance change of various Rh6G solutions at 664 nm before and after degradation. The degradation (%) and reaction rate constant (min^{-1}) are defined as $(1 - \frac{c}{c_0}) \times 100$ and $-\ln(\frac{c}{c_0})/t$; where c, c$_0$, and t refer to the current and initial concentrations of the Rh6G solution and the effective reaction time required for all the solution to flow from the inlet to the outlet, respectively. The degradation of Rh6G within the microreactor channel was simulated by computational fluid dynamic modeling using COMSOL Multiphysics 5.4 (COMSOL Inc., Stockholm, Sweden).

The detailed numerical experiment conditions are given in sections corresponding to the Figs. 4 and 5.

To study the capability of the herringbone microreactor, photocatalytic degradation of various aquatic pollutants, 0.05 M Methyl orange (MO, Sigma-Aldrich) cationic dye, 30 μM Sulfamethoxazole (SMX, Sigma-Aldrich), and standard polystyrene latex suspension (Malvern, USA, 0.1 μm), were tested. The degraded MO solutions were analyzed with their absorption spectra using a UV-Vis spectrophotometer. For the analysis of the degraded SMX solutions, a 1260 Infinity II Prep- high-performance liquid chromatography (HPLC) System (Agilent Technologies, Santa Clara, CA, USA) and an EC-C18 column (4.6×150 mm, Agilent Technologies) were used. The detailed HPLC conditions were as follows: 60:40 0.1% phosphoric acid/acetonitrile (v/v) mobile phase, 10 μL injection volume, 25 °C temperature, and 0.8 mL/min flow rate. The SMX peak at a retention time of 2.89 min was detected with a UV/Vis detector at 270 nm, and the height of the peak was measured for SMX analysis. The degradation of the PS microparticles was analyzed by measuring the average diameter of the particles based on SEM images.

Reporting summary

Further information on research design is available in the Nature Research Reporting Summary linked to this article.

DATA AVAILABILITY

Data generated and analyzed during this study are included in this published article and raw data used for this manuscript are available from the corresponding author within the reasonable request.

CODE AVAILABILITY

Code used in this study is available from the corresponding author within the reasonable request.

REFERENCES

1. Lei, L. et al. Optofluidic planar reactors for photocatalytic water treatment using solar energy. Biomicrofluidics 4, 043004 (2010).
2. Shannon, M. A. et al. Science and technology for water purification in the coming decades. Nature 452, 301–310 (2008).
3. Kim, K., Kim, H., Lim, J. H. & Lee, S. J. Development of a desalination membrane bioinspired by mangrove roots for spontaneous filtration of sodium ions. ACS Nano 10, 11428–11433 (2016).
4. Herrmann, J.-M. Heterogeneous photocatalysis: fundamentals and applications to the removal of various types of aqueous pollutants. Catalysis Today 53, 115–129 (1999).
5. Aarthi, T. & Madras, G. Photocatalytic degradation of rhodamine dyes with nano-TiO2. Ind. Eng. Chem. Res. 46, 7–14 (2007).
6. Markowska-Szczupak, A., Ulfig, K. & Morawski, A. The application of titanium dioxide for deactivation of bioparticulates: an overview. Catalysis Today 169, 249–257 (2011).
7. Horváth, E. et al. Solar water purification with photocatalytic nanocomposite filter based on TiO2 nanowires and carbon nanotubes. npj Clean Water 5, 1–11 (2022).
8. Lv, M. et al. Optimized porous rutile TiO 2 nanorod arrays for enhancing the efficiency of dye-sensitized solar cells. Energy Environ. Sci. 6, 1615–1622 (2013).
9. Kerkez, Ö. & Boz, İ. Efficient removal of methylene blue by photocatalytic degradation with TiO 2 nanorod array thin films. React. Kinet. Mech. Catal. 110, 543–557 (2013).
10. Li, L., Tang, D., Song, Y. & Jiang, B. Dual-film optofluidic microreactor with enhanced light-harvesting for photocatalytic applications. Chem. Eng. J. 339, 71–77 (2018).
11. Li, L. et al. A cascading gradient pore microstructured photoanode with enhanced photoelectrochemical and photocatalytic activities. J. Catalysis 344, 411–419 (2016).
12. Meng, Z., Zhang, X. & Qin, J. A high efficiency microfluidic-based photocatalytic microreactor using electrospun nanofibrous TiO2 as a photocatalyst. Nanoscale 5, 4687–4690 (2013).
13. Farrugia, C. et al. Suitability of different titanium dioxide nanotube morphologies for photocatalytic water treatment. Nanomaterials 11, 708 (2021).
14. Shaheen, S. et al. Graphene oxide-ZnO nanorods for efficient dye degradation, antibacterial and in-silico analysis. Appl. Nanosci. 12, 165–177 (2022).
15. Rajeshwari, M. R., Kokilavani, S. & Khan, S. S. Recent developments in architecturing the g-C3N4 based nanostructured photocatalysts: synthesis, modifications and applications in water treatment. Chemosphere 291, 132735 (2021).
16. Parmar, J., Jang, S., Soler, L., Kim, D.-P. & Sánchez, S. Nano-photocatalysts in microfluidics, energy conversion and environmental applications. Lab Chip 15, 2352–2356 (2015).
17. Wang, N., Zhang, X., Wang, Y., Yu, W. & Chan, H. L. Microfluidic reactors for photocatalytic water purification. Lab Chip 14, 1074–1082 (2014).
18. Monat, C., Domachuk, P. & Eggleton, B. Integrated optofluidics: a new river of light. Nat. Photonics 1, 106–114 (2007).
19. Nagamine, S. & Inohara, K. Photocatalytic microreactor using anodized TiO2 nanotube array. Adv. Powder Technol. 29, 3100–3106 (2018).
20. Jing, W. et al. Regulation of the volume flow rate of aqueous methyl blue solution and the wettability of CuO/ZnO nanorods to improve the photodegradation performance of related microfluidic reactors. Langmuir 37, 7890–7906 (2021).
21. Li, L. et al. Optofluidics based micro-photocatalytic fuel cell for efficient wastewater treatment and electricity generation. Lab Chip 14, 3368–3375 (2014).
22. Yusuf, A., Garlisi, C. & Palmisano, G. Overview on microfluidic reactors in photocatalysis: applications of graphene derivatives. Catal. Today 315, 79–92 (2018).
23. Yu, G. & Wang, N. Gas-Liquid-Solid interface enhanced photocatalytic reaction in a microfluidic reactor for water treatment. Appl. Catal. A Gen. 591, 117410 (2020).
24. Nagamine, S. Photocatalytic microreactor using TiO2/Ti plates: formation of TiO2 nanostructure and separation of oxidation/reduction into different channels. Adv. Powder Technol. 31, 521–527 (2020).
25. Grao, M., Ratova, M. & Kelly, P. Design and optimisation of a low-cost titanium dioxide-coated stainless steel mesh photocatalytic water treatment reactor. J. Clean. Prod. 297, 126641 (2021).
26. Xiao, M. et al. Hollow nanostructures for photocatalysis: advantages and challenges. Adv. Mater. 31, 1801369 (2019).
27. Wang, W. & Qi, L. Light management with patterned micro-and nanostructure arrays for photocatalysis, photovoltaics, and optoelectronic and optical devices. Adv. Funct. Mater. 29, 1807275 (2019).
28. Hessel, V., Löwe, H. & Schönfeld, F. Micromixers—a review on passive and active mixing principles. Chem. Eng. Sci. 60, 2479–2501 (2005).
29. Nam-Trung, N. & Zhigang, W. Micromixers—a review. J. Micromech. Microeng. 15, R1–R16 (2004).
30. Liao, Y. et al. Rapid prototyping of three-dimensional microfluidic mixers in glass by femtosecond laser direct writing. Lab Chip 12, 746–749 (2012).
31. Therriault, D., White, S. R. & Lewis, J. A. Chaotic mixing in three-dimensional microvascular networks fabricated by direct-write assembly. Nat. Mater. 2, 265–271 (2003).
32. Howell, P. B. Jr. et al. A microfluidic mixer with grooves placed on the top and bottom of the channel. Lab Chip 5, 524–530 (2005).
33. Liu, R. H. et al. Passive mixing in a three-dimensional serpentine microchannel. J. Microelectromechan. Syst. 9, 190–197 (2000).
34. Stroock, A. D. et al. Chaotic mixer for microchannels. Science 295, 647–651 (2002).
35. Lin, D. et al. Three-dimensional staggered herringbone mixer fabricated by femtosecond laser direct writing. J. Opt. 15, 025601 (2013).
36. Ansari, M. A. & Kim, K.-Y. Shape optimization of a micromixer with staggered herringbone groove. Chem. Eng. Sci. 62, 6687–6695 (2007).
37. Pino, E., Calderón, C., Herrera, F., Cifuentes, G. & Arteaga, G. Photocatalytic degradation of aqueous rhodamine 6G using supported TiO2 catalysts. A model for the removal of organic contaminants from aqueous samples. Front. Chem. 8, 365 (2020).
38. da Silva, A. M. B. et al. Removal of rhodamine 6G from synthetic effluents using Clitoria fairchildiana pods as low-cost biosorbent. Environ. Sci. Pollut. Res. 27, 2868–2880 (2020).
39. Kwon, H., Lee, S. H. & Kim, J. K. Three-dimensional metal-oxide nanohelix arrays fabricated by oblique angle deposition: fabrication, properties, and applications. Nanoscale Res. Lett. 10, 1–12 (2015).
40. Hwang, S. et al. A near single crystalline TiO 2 nanohelix array: enhanced gas sensing performance and its application as a monolithically integrated electronic nose. Analyst 138, 443–450 (2013).
41. Ho, Y.-C. et al. Enhancing performance of inverted polymer solar cells using two-growth ZnO nanorods. Sol. Energy Mater. Sol. Cells 132, 570–577 (2015).
42. Magde, D., Elson, E. L. & Webb, W. W. Fluorescence correlation spectroscopy. II. An experimental realization. Biopolymers 13, 29–61 (1974).

43. Lin, H. & Valsaraj, K. T. Development of an optical fiber monolith reactor for photocatalytic wastewater treatment. *J. Appl. Electrochem.* **35**, 699–708 (2005).

44. Lopez, L., Daoud, W. A., Dutta, D., Panther, B. C. & Turney, T. W. Effect of substrate on surface morphology and photocatalysis of large-scale TiO$_2$ films. *Appl. Surf. Sci.* **265**, 162–168 (2013).

45. Osminkina, L. A. et al. Optical properties of silicon nanowire arrays formed by metal-assisted chemical etching: evidences for light localization effect. *Nanoscale Res. Lett.* **7**, 1–6 (2012).

46. Lide, D. R. *CRC Handbook of Chemistry and Physics*. (CRC, Boca Raton, 2008).

47. Fang, Y. et al. Plasmon enhanced internal photoemission in antenna-spacer-mirror based Au/TiO2 nanostructures. *Nano Lett.* **15**, 4059–4065 (2015).

48. Qamar, M., Gondal, M. & Yamani, Z. Removal of Rhodamine 6G induced by laser and catalyzed by Pt/WO3 nanocomposite. *Catal. Commun.* **11**, 768–772 (2010).

49. Zhang, F. et al. Ordered mesoporous Ag–TiO 2–KIT-6 heterostructure: synthesis, characterization and photocatalysis. *J. Mater. Chem.* **19**, 2771–2777 (2009).

50. Kwon, H., Sung, J. H., Lee, Y., Jo, M.-H. & Kim, J. K. Wavelength-dependent visible light response in vertically aligned nanohelical TiO2-based Schottky diodes. *Appl. Phys. Lett.* **112**, 043106 (2018).

51. Hassell, D. & Zimmerman, W. Investigation of the convective motion through a staggered herringbone micromixer at low Reynolds number flow. *Chem. Eng. Sci.* **61**, 2977–2985 (2006).

52. Abellán, M., Bayarri, B., Giménez, J. & Costa, J. Photocatalytic degradation of sulfamethoxazole in aqueous suspension of TiO2. *Appl. Catal. B: Environ.* **74**, 233–241 (2007).

53. Yuan, R., Zhu, Y., Zhou, B. & Hu, J. Photocatalytic oxidation of sulfamethoxazole in the presence of TiO2: Effect of matrix in aqueous solution on decomposition mechanisms. *Chem. Eng. J.* **359**, 1527–1536 (2019).

54. Nabi, I. et al. Complete photocatalytic mineralization of microplastic on TiO2 nanoparticle film. *Iscience* **23**, 101326 (2020).

55. Liao, J. et al. Photocatalytic degradation of methyl orange using a TiO2/Ti mesh electrode with 3D nanotube arrays. *ACS Appl. Mater. Interfaces* **4**, 171–177 (2012).

56. Shang, J., Chai, M. & Zhu, Y. Photocatalytic degradation of polystyrene plastic under fluorescent light. *Environ. Sci. Technol.* **37**, 4494–4499 (2003).

57. Allé, P. H., Garcia-Muñoz, P., Adouby, K., Keller, N. & Robert, D. Efficient photo-catalytic mineralization of polymethylmethacrylate and polystyrene nanoplastics by TiO2/β-SiC alveolar foams. *Environ. Chem. Lett.* **19**, 1803–1808 (2021).

58. Ioannidou, E. et al. Solar photocatalytic degradation of sulfamethoxazole over tungsten–Modified TiO2. *Chem. Eng. J.* **318**, 143–152 (2017).

59. Hawkeye, M. M. & Brett, M. J. Glancing angle deposition: fabrication, properties, and applications of micro-and nanostructured thin films. *J. Vac. Sci. Technol. A* **25**, 1317–1335 (2007).

ACKNOWLEDGEMENTS

AUTHOR CONTRIBUTIONS
H. Kim, H. Kwon, P.F., and E.B. conceived and plan the presented idea. H. Kim and H. Kwon equally contribute to the study. H. Kim, H. Kwon, S.S., S.-Y.H., and H.-D.P. carried out the experiment and analysed the data. R.S. and J.L. performed the numerical simulations and analyzed the data. All authors contributed to the interpretation of the results. H. Kim took the lead in writing the manuscript, and all authors contributed to the final version of the manuscript.

FUNDING

COMPETING INTERESTS
The authors declare no competing interests.

ADDITIONAL INFORMATION
Supplementary information The online version contains supplementary material available at https://doi.org/10.1038/s41545-022-00204-y.

Correspondence and requests for materials should be addressed to Hyejeong Kim.

Reprints and permission information is available at http://www.nature.com/reprints

Publisher's note Springer Nature remains neutral with regard to jurisdictional claims in published maps and institutional affiliations.